

Origin of the narrow, single peak in the fission-fragment mass distribution for ^{258}Fm

Takatoshi Ichikawa,¹ Akira Iwamoto,² and Peter Möller³

¹*RIKEN Nishina Center, RIKEN, Wako, Saitama 351-0198, Japan*

²*Japan Atomic Energy Agency, Tokai-mura, Naka-gun, Ibaraki 319-1195, Japan*

³*Theoretical Division, Los Alamos National Laboratory, Los Alamos, New Mexico 87545, USA*

(Dated: October 26, 2018)

We discuss the origin of the narrowness of the single peak at mass-symmetric division in the fragment mass-yield curve for spontaneous fission of ^{258}Fm . For this purpose, we employ the macroscopic-microscopic model, and calculate a potential-energy curve at the mass-symmetric compact scission configuration, as a function of the fragment mass number, which is obtained from the single-particle wave-function densities. In the calculations, we minimize total energies by varying the deformations of the two fragments, with constraints on the mass quadrupole moment and keeping the neck radius zero, as a function of mass asymmetry. Using the obtained potential, we solve the one-dimensional Schrödinger equation with a microscopic coordinate-dependent inertial mass to calculate the fragment mass-yield curve. The calculated mass yield, expressed in terms of the microscopic mass density, is consistent with the extremely narrow experimental mass distribution.

PACS numbers: 24.75.+i, 27.90.+b

In spontaneous fission the fragment mass-yield distributions change abruptly from a double-peaked, broad, mass-asymmetric distribution for ^{256}Fm to a single-peaked, very narrow, symmetric distribution for ^{258}Fm [1, 2, 3]. In addition, in ^{258}Fm the kinetic-energy distribution can be expressed as a sum of a low-energy and a high-energy component, whose mean energies differ by about 35 MeV. The mechanism behind this phenomenon, called bimodal fission, is the strong nuclear shell effects that appear when symmetric division into two fragments which both are near the doubly magic nucleus ^{132}Sn becomes possible. The experimental observations of the sudden emergence of a mass-symmetric division near ^{258}Fm has always been assumed to be due to an emergence in fission potential-energy surfaces of a fission path, strongly stabilized by fragment shell effects [1, 4, 5, 6, 7]. However, no such intuitive picture of the mechanism behind the narrowness of the symmetric mass distribution peak has been advanced, nor has a convincing quantitative calculation explaining the extremely narrow FWHM been presented.

So far, theoretical investigations have mainly focused on obtaining the transition point between competing fission modes near ^{258}Fm by calculating the potential-energy surface versus various chosen sets of deformation coordinates. In fact, theoretical models, such as the macroscopic-microscopic model [8, 9, 10, 11, 12, 13], the constrained Hartree-Fock+BCS (HFBCS) model [14, 15], and the constrained Hartree-Fock-Bogoliubov (HFB) model [16, 17], have to a varying degree of success described such a shell-stabilized path, and the transition point between asymmetric and symmetric fission modes near ^{258}Fm , that is, the emergence here of path leading to mass-symmetric divisions with compact scission configurations, referred to as the compact symmetric path. Through these investigations the energy-minimum path leading to high-kinetic-energy, symmetric fission has been well established, but the structure of the *potential valley* along this path and plausible mechanisms behind the extremely narrow FWHM have been less extensively studied.

In this paper, we calculate quantitatively the mass distribution of ^{258}Fm in the compact symmetric valley. The calcula-

tions are based on studies of the dynamics of the zero-neck-radius scission configuration in the mass-asymmetry shape degree of freedom [18]. We also impose spherical fragment shapes, which leaves us with mass asymmetry as the only collective coordinate. This approach implies that the mass distribution originates from zero-point vibrations or thermal fluctuations in the mass-asymmetry degree of freedom at scission. In the specific case of ^{258}Fm considered here, it is a reasonable assumption and approximation, since in spontaneous fission the exit point after barrier penetration is approximately the zero-neck scission configuration.

We use the macroscopic-microscopic model [19, 20] constrained to shapes with zero neck radius. Using a macroscopic-microscopic model, slightly different from our implementation, Pashkevich failed to find any significant difference between the curvatures of the compact and elongated symmetric valleys for ^{264}Fm [9]. Furthermore, in his cranking-model analysis of the mass distribution widths associated with the zero-point oscillations in his asymmetry degree of freedom he obtained similar mass yield distribution widths in both valleys, approximately consistent with the narrow distribution observed experimentally for ^{258}Fm . His dynamical study has significant similarities with our study here. However, Pashkevich characterized fragment mass numbers by the asymmetry of the homogeneous macroscopic volume defined by the parametrization of the nuclear surface. Here we use microscopic densities to characterize the mass distribution, which gives very different mass-distribution curves close to magic numbers. As we discuss in detail below, we propose it is the shell gaps that restrict fluctuations in the microscopic mass-asymmetry degree of freedom.

We use the three-quadratic-surface parametrization [21, 22] to describe macroscopic nuclear shapes in a five-dimensional deformation space. The shape degrees of freedom are a quadrupole-moment parameter q_2 , a neck parameter η , left- and right-fragment deformation parameters, ε_1 and ε_2 , respectively, and a mass-asymmetry parameter α_g . The parameter q_2 is the dimensionless quadrupole moment in units of $3ZR_0^2/4\pi$ (e^2b), where Z is the proton number and R_0

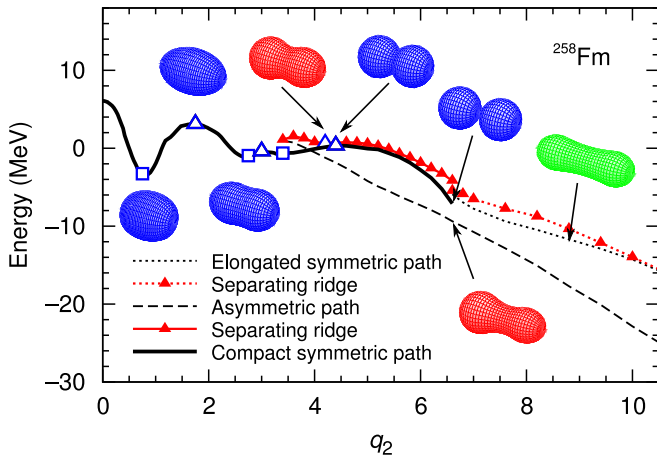


FIG. 1: (Color online) Potential energy as a function of the dimensionless quadrupole moment parameter q_2 . The open squares and triangles are the minima and optimal saddles obtained by the immersion method in the five-dimensional potential-energy surface, respectively. The solid and dotted lines are the valleys leading to compact and elongated symmetric fission. The dashed line is the valley leading to the asymmetric fission. The solid and dotted lines with triangles represent the separation ridge between the compact symmetric and the asymmetric valleys and the separating ridge between the elongated symmetric and the asymmetric valleys, respectively.

is the nuclear radius. The parameter η varies from 0 to 1. Scission, with zero neck radius, corresponds to $\eta = 0$. The parameter ε is the Nilsson perturbed-spheroid parameter. Near scission we have to a very good approximation $\alpha_g = (M_1 - M_2)/(M_1 + M_2)$, where M_1 and M_2 are the volumes of the left and right nascent fragments, respectively. The microscopic single-particle potential is calculated by folding a Yukawa function over the macroscopic shape or “sharp-surface generating volume” [19].

To study the properties of the compact, mass-symmetric valley, we calculate the five-dimensional potential-energy surface for ^{258}Fm and analyze it by use of the immersion method. Details of the calculation are given in Ref. [23]. The parameters correspond to FRLDM(2002) [24]. For simplicity, we calculate the pairing effect based on the BCS model [25]. Since we mainly consider scission or near-scission shapes, we can ignore the shape dependence of the Wigner term. We calculate the potential energies at $41 \times 20 \times 15 \times 15 \times 35$ grid points for Q_2 , η , ε_1 , ε_2 , and α_g , respectively.

Figure 1 shows some main structures identified by immersion techniques in the calculated potential-energy surface for ^{258}Fm as a function of q_2 . The open squares and triangles are minima and optimal saddles between minima, respectively. The energy of the saddle point on the path to compact symmetric fission is 0.34 MeV, while that of the asymmetric fission is 0.58 MeV. The scission point for the compact symmetric fission is at $q_2 = 6.5$, $\varepsilon_{1,2} = 0$, and $a_g = 0$. In the figure, we show the compact symmetric and the asymmetric valleys, denoted by a solid and a dashed line, respectively. Those are separated by a ridge, denoted by a solid line with triangles. We also find a path leading to elongated mass-symmetric di-

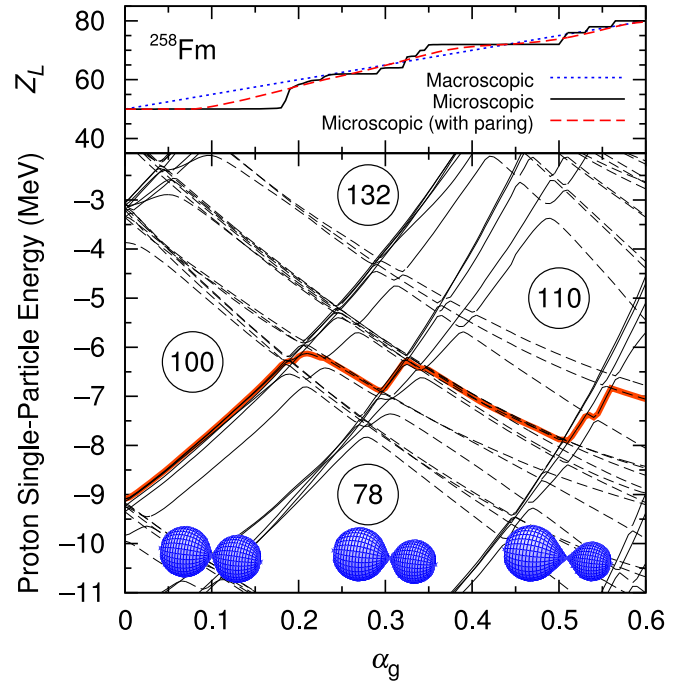


FIG. 2: (Color online) (Upper panel) Proton number of left fragment as a function of the mass-asymmetric parameter α_g . The solid line is the total proton density obtained as a sum over occupied wave functions in the left fragment. The dashed line is the total proton density with pairing taken into account. The dotted line is the macroscopic left-fragment density. (Lower panel) Nilsson diagram for proton single-particle levels at scission configurations in the compact symmetric valley as a function of the mass-asymmetric parameter α_g . The solid and dashed lines are the energy levels whose wave function localizes in the right- and left fragments, respectively. The bold-gray (red) line is the Fermi level.

visions, denoted by a dotted line, but its separating ridge to the asymmetric valley, denoted by the dotted line with triangles, vanishes at around $q_2 = 10.0$, indicating that the scission point of this path strongly depends on the dynamics after going through this valley.

Before we discuss the dependence of the potential energy on mass asymmetry at the compact scission configuration we need to discuss the relation between fragment mass numbers and single-particle energy levels. For this purpose, we calculate the proton density for each single-particle state and the total proton number of the left fragment as a function of α_g . For $\alpha_g > 0$, the volume of the left fragment is greater than the right fragment. We take ε_1 and ε_2 to be 0 in the calculation. If we maintain our restriction to axially symmetric shapes, the proton density for the i -th single-particle state is given by $|\psi_i(\rho, z)|^2$, where ψ is the single-particle wave function in the cylindrical coordinate system. The single-proton occupation probability in left of two nascent fragments is thus obtained by

$$n_i = 2\pi \int_0^{\rho_{\max}} \int_{z_{\min}}^{z_{\text{neck}}} \rho |\psi_i(\rho, z)|^2 dz d\rho, \quad (1)$$

where z_{neck} is at a macroscopic neck radius of 0 fm. The

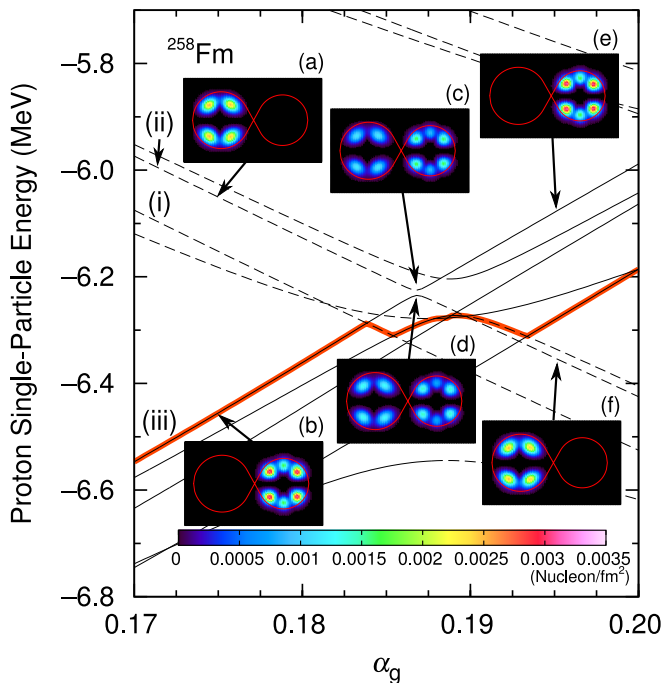


FIG. 3: (Color online) Enlargement of part of Fig. 2 with density plots of a few specific wave functions discussed in the text. In the insets, the corresponding macroscopic nuclear shape is given by the solid line.

values ρ_{\max} and z_{\min} (negative) are set sufficiently large that $|\psi_i(\rho, z)|^2$ becomes negligible outside the integration intervals. The total proton number Z_L is the sum of the single-proton occupation probability from the lowest level to the Fermi level. We also calculate the total proton number taking into account the pairing effect, $Z_L^{(\text{BCS})}$, given by $Z_L^{(\text{BCS})} = \sum v_i^2 n_i$, where v_i^2 is the occupation probability calculated using the BCS pairing model.

We use two density concepts when we discuss the mass asymmetry in our study. One definition is based on calculating the mass asymmetry from the single-particle densities, the other from the asymmetry of the homogeneous volume defined by the parametrization of the nuclear surface, denoted “microscopic” and “macroscopic”, respectively.

Figure 2 shows important features of our results. The solid and dashed lines in the upper panel of Fig. 2 show the total number of protons without and with the pairing effects, Z_L and $Z_L^{(\text{BCS})}$, respectively. The lower panel of Fig. 2 is a Nilsson diagram versus α_g . The thick gray (red) line is the Fermi level. The energy levels are plotted dashed when more than half the density is in the left part of the potential, solid otherwise [see the insets from (a) to (f) in Fig. 3]. The upper panel shows that in the absence of pairing the total proton number remains constant at $Z_L = 50$ in the interval $0 \leq \alpha_g \leq 0.18$. Just below $\alpha_g = 0.20$, Z_L suddenly jumps to about 60. One can also see such discontinuities at large α_g . Those discontinuities occur where single-particle shell gaps change, that is they coincide with the level crossing points in the Nilsson diagram. It is here the downward-sloping states whose wave

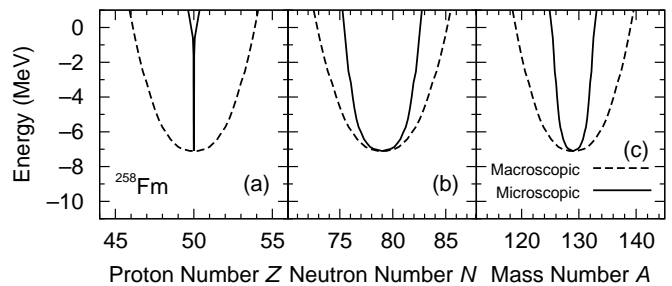


FIG. 4: Potential-energy curves at the scission configuration as a function of the (a) proton, (b) neutron, and (c) total mass densities of two nascent fragments, respectively. The solid and dashed lines denote the potential-energy curve calculated using the microscopic and macroscopic densities, respectively.

functions are localized in the left fragment come below the Fermi level and can be populated with particles transferring from the right fragment. These sudden features are smoothed out when we include the pairing correlation.

In order to see more clearly how Z_L increases we show in Fig. 3 an enlargement of the Fermi-surface region of Fig. 2, with some wave-function densities inserted. In the figure, the downward-sloping state denoted by the line (i), coming from above the Fermi level, dives below the Fermi level. In the case we have here with paired particles, protons can transfer from the right fragment into this previously unoccupied state in the left fragment, which leads to an increase of Z_L . In contrast, in the case the particle number is odd then the odd particle can not transfer to a level of different Ω , in a sudden shape change. Rather, the odd particle remains in its level until another level with the same Ω quantum number is encountered, giving rise to a “specialization energy” and an increase in barrier height. This is the mechanism behind the long spontaneous fission half-lives of odd nuclei [26, 27]. When a downward sloping level encounters an upward-sloping level of the same quantum number Ω when it crosses the Fermi surface, then a repulsion between the single-particle states occurs. This is the case for the states denoted by (ii) and (iii), which have the same quantum number, $\Omega = 5/2$, but their wave functions localize on the right- and left fragments, respectively [see the insets (a) and (b) in Fig. 3]. The transfer mechanism in the even, paired system is similar to case (i), but in the single-particle picture it appears different because when these states come close to each other the states mix (“level repulsion”), in this case near $\alpha_g = 0.185$ [see the insets (c) and (d)]. After the mixing region, the localizations of the wave functions are interchanged [see the insets (e) and (f)], and the lower level remains below the Fermi level, but with a new set of quantum numbers. This microscopic mechanism is responsible for the increase in Z_L with increasing α_g .

As shown by the dashed line in the upper panel of Fig. 2, the pairing interaction smooths the change in the fragment proton number versus asymmetry, because it incorporates wave-function admixtures across the single-particle Fermi surface into the sum of the single-proton densities. As a consequence, if the density of states just above a shell gap occurring at

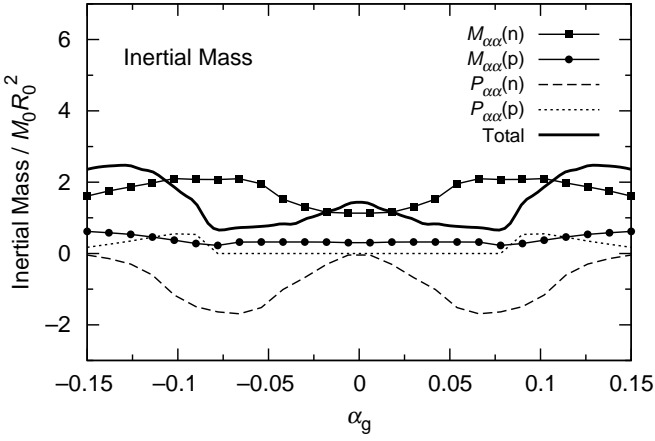


FIG. 5: Inertial mass in the mass-asymmetric direction at the compact-symmetric scission configuration calculated using the Inglis-Belyaev formula. The solid lines with squares and circles are the first term of the RHS in Eq. 3 for neutrons and protons, respectively. The dashed and dotted lines are the second term of the RHS in Eq. 3 for neutrons and protons, respectively. The solid line is the total inertial mass for neutrons and protons calculated as the sum of the first and second terms in Eq. 3.

the Fermi surface is high, then $Z_L^{(\text{BCS})}$ more closely tracks the macroscopic proton number. At large a_g this condition is particularly well fulfilled and the dashed line is close to the macroscopic density, denoted by the dotted line in the figure. However, we found that from $\alpha_g = 0$ to 0.10, $Z_L^{(\text{BCS})}$ still remains constant at 50 due to the very substantial shell gap, indicating that proton number $Z = 50$ is extremely stable. We will show below that this stability may to a large part be the mechanism that leads the very narrow fragment mass distribution.

We now calculate the potential-energy curve at the scission configuration in the compact symmetric valley as a function of the fragment mass number. In this first study we take ε_1 and ε_2 to be zero in calculating the potential energy and the inertial mass. We have checked this approximation by minimizing the total energy with respect to ε_1 and ε_2 with constraints on $q_2 = 6.5$ and a neck radius of 0 fm, as α_g increases. From $\alpha_g = 0$ to 0.1, we found that the minimum energy occurs at ε_1 and ε_2 equal zero due to the large spherical shell gap, but abruptly jumps to other valleys near $\alpha_g = 0.1$. Inaccuracies due to this approximation can therefore be expected to be fairly insignificant. We calculated the fragment mass number using the single-particle wave functions with the BCS pairing effect, before this jump takes place.

Figures 4 (a), (b), and (c) show calculated potential energies as functions of the fragment microscopic proton, neutron, and total mass densities, respectively. These results are given by the solid lines. As a comparison, results versus the macroscopic density are also given, displayed as dashed lines. The potential-energy curves versus the microscopic density rise much more steeply than the curves plotted versus the macroscopic density. In particular, the result versus the proton density depends drastically on the choice of density variable. We

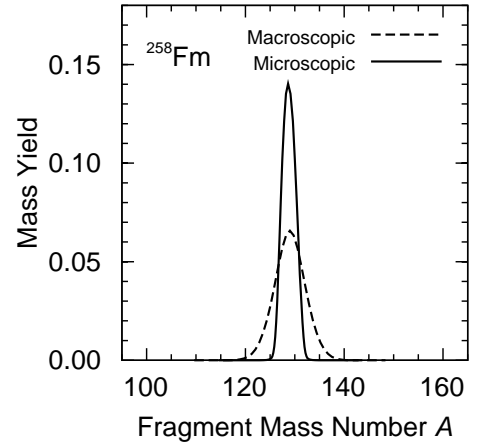


FIG. 6: Calculated mass-yield curves for compact fission of ^{258}Fm . The solid and dashed lines are based on the microscopic and macroscopic densities, respectively.

therefore expect that the physical origin of the narrow mass distribution is the large shell gap. Below we investigate this hypothesis through a quantitative study.

In order to calculate the mass distribution in the compact symmetric mode, we calculate the zero-point vibration corresponding to the calculated potential-energy curves displayed in Fig. 4, by solving the one-dimensional Schrödinger equation in terms of α_g with a coordinate-dependent inertial mass [28]. For the compact symmetric valley, we expect the zero-point vibration to be dominating, because the observed excitation energy of the fission fragments of the nearby ^{260}Md in compact, symmetric fission was extremely low [29]. The Schrödinger equation thus reads

$$\left[-\frac{\hbar^2}{2\sqrt{B}} \frac{\partial}{\partial \alpha_g} \frac{1}{\sqrt{B}} \frac{\partial}{\partial \alpha_g} + V(\alpha_g) \right] \psi(\alpha_g) = E \psi(\alpha_g), \quad (2)$$

where ψ is the wave function and B is the inertial mass in the mass-asymmetric direction $B_{\alpha\alpha}$.

For the inertial mass, we employ the Inglis-Belyaev formula [30, 31], given by

$$B_{\alpha\alpha} = 2\hbar^2 \left[\sum_{\nu\mu} \frac{|\langle \nu | \partial H / \partial \alpha | \mu \rangle|^2 (u_\nu v_\mu + u_\mu v_\nu)^2}{(E_\nu + E_\mu)^3} \right] + P_{\alpha\alpha}, \quad (3)$$

where H is the single-particle Hamiltonian, v_μ and u_μ are the BCS occupancy and vacancy amplitudes, and E_μ is the energy of the quasi-particle state $|\mu\rangle$. The term $P_{\alpha\alpha}$ gives the contribution from couplings to the pairing vibrations. We use the finite-difference method to calculate $\langle \mu | \partial H(\alpha) / \partial \alpha | \nu \rangle$. Figure 5 shows the calculated inertial mass in units of $M_0 R_0^2$, where $M_0 = 931.50$ MeV is the atomic mass unit. The solid lines with squares and circles show the evaluated first term in the right hand side of Eq. 3 for the neutrons and the protons, respectively. The dashed and dotted lines show the evaluated $P_{\alpha\alpha}$ for neutrons and protons, respectively. The solid line is the sum of those four terms.

We calculate $\psi(\alpha_g)$ in Eq. 2 using the finite-difference method. The calculated zero-point energy is -6.05 MeV. The

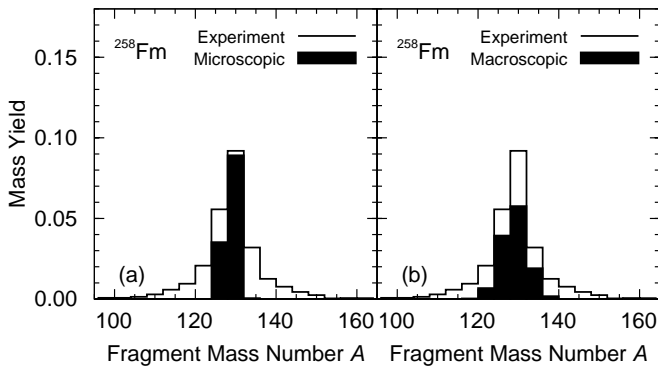


FIG. 7: Mass yields plotted in histogram form. The black-shaded histograms in the figures (a) and (b) are calculated mass yields using the microscopic and the macroscopic densities, respectively. The solid-line histograms are experimental data taken from Ref. [32].

calculated $\psi(\alpha_g)$, which is the macroscopic density amplitude, is converted into a mass yield function $Y(A)$ in terms of fragment microscopic densities through, $Y(A) = C|\psi(A)|^2$, where C is a renormalization factor. We chose C so that the total area of Y is equal to 0.5, because the component originating from the compact symmetric valley is about 50% of the total yield. This has been estimated from the two-mode analysis of the experimental total kinetic-energy distribution [3]. The structure of our calculated potential-energy surface is consistent with this assumption, because the calculated height of the saddle point leading to the compact symmetric valley is comparable to that of the asymmetric valley. See also Refs. [12, 23].

Figure 6 shows the macroscopic and microscopic mass-yield curves. The same data are shown as histograms in Fig. 7, so that we can compare directly to the experimental data, which are given in histogram form [32]. In transforming to the histograms, we calculate the average of integrated values of the mass-yield curve for the 4 u interval used in the presentation of the experimental data [32]. The solid and the dashed lines in Fig. 6 correspond to the microscopic and the macroscopic densities, respectively. The calculated peak value is consistent with the experimental one, although a one-dimensional model could have a tendency to overestimate the peak value of the mass-yield curve [28]. On the other hand, it is clearly seen that the result of the macroscopic density is not in agreement with the extremely narrow peak of the experimental mass-yield curve. That is, the single-particle configuration, and specifically the large shell gap, is the source of the extremely narrow FWHM of the fragment mass-yield curve. We thus expect that the FWHM of the compact symmetric component is 3.6 u.

In order to obtain the whole mass distribution, it would be necessary to clarify valley structures for all fission paths and superpose their contributions. However, we could not employ our scission-point model to the other valleys, because it was not possible to obtain unique scission points for the asymmetric and elongated symmetric paths. For those paths the separating ridge vanishes before the scission configurations, indicating that these components must be modeled in a more

complex dynamical approach.

One may ask how the features we studied here manifest themselves in self-consistent mean-field calculations which have also studied ^{258}Fm . In those models the potential and microscopic densities are “self-consistent”. One could anticipate that perhaps no self-consistent solutions exist for octupole constraints corresponding to the range 0 to 0.18 of α_g in Fig. 2. And when a solution exists there would be a large increase in energy. If these expectations do occur in self-consistent models this behavior would tend to very much restrict the fluctuations in the mass-yield curve, just like in our studies here. However, in the papers [14, 17] we find no results that shed light on precisely these issues. But the calculated barrier versus a quadrupole constraint in [14] is very similar to the barrier obtained here. Recently [17] looked at correlations between various fission fragment properties of Fm isotopes. These calculations do not clearly identify any fragment shell effect on mass yield widths. This is probably because they were not specifically designed to study such a possibility. In Ref. [17], the Hartree-Fock-Bogoliubov method is used to calculate potential-energy surfaces of Fm isotopes along a scission line. The results for the ^{258}Fm potential energy shown in Fig. 7 have quite different shape compared to our Fig. 4(c). In particular the potential shows a very shallow minimum centered at symmetric division. The comparisons of calculated total kinetic energies to data is not very convincing. The substantially different results we obtain are likely due to the very different designs of the two studies, not to the differences between self-consistent and non-selfconsistent models. In our case we study mass oscillations near the exit point of compact scission. In the HFB study energy partitioning along the entire scission line is the mechanism governing the fragment properties. Since that mechanism shows substantial differences with respect to measured data, we feel it is more appropriate to describe origin of the narrow mass distribution in terms of the large shell gap at the barrier exit point, as we do here.

In summary, we have presented potential-energy curves of ^{258}Fm at scission as functions of both macroscopic and microscopic fragment mass densities. We calculated the zero-point vibration corresponding to this potential-energy curve by solving a one-dimensional Schrödinger equation with a coordinate-dependent inertial mass based on the cranking model. An important point in the calculation is that the fragment masses are defined by the single-particle wave functions, rather than the macroscopic potential volumes. We have shown that the mass numbers of two nascent fragments strongly depend on the single-particle configurations. In particular, the proton number of the fission fragments originating from the compact symmetric valley for ^{258}Fm is strongly constrained to $Z = 50$ due to the large shell gap. The calculated mass-yield curve is consistent with the extremely narrow experimental mass yield curve. We obtain that the FWHM of the fission fragments originating from the compact symmetric valley is 3.6 u. For ^{258}Fm , it would be interesting to measure the ratio of protons to neutrons on the mass yield curve, because the neutron distribution may be wider than the proton distribution, since the mean fragment neutron number is not magic. This would be a very strong test of the mechanism

behind the narrow mass distribution.

Acknowledgments

TI is grateful for the Special Postdoctoral Researcher Program in RIKEN. The numerical calculations have been performed at the RSCC system, RIKEN. PM would like to ac-

knowledge that this work was carried out under the auspices of the National Nuclear Security Administration of the U.S. Department of Energy at Los Alamos National Laboratory under Contract No. DE-AC52-06NA25396 and was also supported by a travel grant to JUSTIPEN (Japan-U.S. Theory Institute for Physics with Exotic Nuclei) under grant number DE-FG02-06ER41407 (U. Tennessee).

-
- [1] D. C. Hoffman, J. B. Wilhelmy, J. Weber, W. R. Daniels, E. K. Hulet, R. W. Lougheed, J. H. Landrum, J. F. Wild, and R. J. Dupzyk, *Phys. Rev. C* **21**, 972 (1980).
- [2] E. K. Hulet, J. F. Wild, R. J. Dougan, R. W. Lougheed, J. H. Landrum, A. D. Dougan, M. Schadel, R. L. Hahn, P. A. Baisden, C. M. Henderson, et al., *Phys. Rev. Lett.* **56**, 313 (1986).
- [3] E. K. Hulet, J. F. Wild, R. J. Dougan, R. W. Lougheed, J. H. Landrum, A. D. Dougan, P. A. Baisden, C. M. Henderson, R. J. Dupzyk, R. L. Hahn, et al., *Phys. Rev. C* **40**, 770 (1989).
- [4] Y. L. Zhao, I. Nishinaka, Y. Nagame, M. Tanikawa, K. Tsukada, S. Ichikawa, K. Sueki, Y. Oura, H. Ikezoe, S. Mitsuoka, et al., *Phys. Rev. Lett.* **82**, 3408 (1999).
- [5] Y. L. Zhao, Y. Nagame, I. Nishinaka, K. Sueki, and H. Nakahara, *Phys. Rev. C* **62**, 014612 (2000).
- [6] H. C. Britt, D. C. Hoffman, J. van der Plicht, J. B. Wilhelmy, E. Cheifetz, R. J. Dupzyk, and R. W. Lougheed, *Phys. Rev. C* **30**, 559 (1984).
- [7] D. C. Hoffman and M. R. Lane, *Radiochim. Acta* **70/71**, 135 (1995).
- [8] P. Möller, J. R. Nix, and W. J. Swiatecki, *Nuclear Physics A* **469**, 1 (1987).
- [9] V. V. Pashkevich, *Nucl. Phys. A* **477**, 1 (1988).
- [10] P. Möller, J. R. Nix, and W. J. Swiatecki, *Nuclear Physics A* **492**, 349 (1989).
- [11] S. Ćwiok, P. Rozmej, A. Sobczewski, and Z. Patyk, *Nucl. Phys. A* **491**, 281 (1989).
- [12] P. Möller and J. R. Nix, *J. Phys. G: Nucl. Part. Phys.* **20**, 1681 (1994).
- [13] P. Möller, D. G. Madland, A. J. Sierk, and A. Iwamoto, *Nature (London)* **409**, 785 (2001).
- [14] L. Bonneau, *Phys. Rev. C* **74**, 014301 (2006).
- [15] A. Staszczak, J. Dobaczewski, and W. Nazarewicz, *Acta Phys. Pol. B* **38**, 1589 (2007).
- [16] M. Warda, J. L. Egido, L. M. Robledo, and K. Pomorski, *Phys. Rev. C* **66**, 014310 (2002).
- [17] N. Dubray, H. Goutte, and J.-P. Delaroche, *Phys. Rev. C* **77**, 014310 (2008).
- [18] R. Vandenbosch and J. R. Huizenga, *Nuclear fission* (Academic Press, INC., London, 1973).
- [19] M. Bolsterli, E. O. Fiset, J. R. Nix, and J. L. Norton, *Phys. Rev. C* **5**, 1050 (1972).
- [20] P. Möller, J. R. Nix, W. D. Myers, and W. J. Swiatecki, *At. Data Nucl. Data Tables* **59**, 185 (1995).
- [21] J. R. Nix, University of California Radiation Laboratory Report UCRL-17958 (1968).
- [22] J. R. Nix, *Nucl. Phys. A* **130**, 241 (1969).
- [23] P. Möller, A. J. Sierk, T. Ichikawa, A. Iwamoto, R. Bengtsson, H. Uhrenholt, and S. Åberg, to be published.
- [24] P. Möller, A. J. Sierk, and A. Iwamoto, *Phys. Rev. Lett.* **92**, 072501 (2004).
- [25] P. Möller and J. R. Nix, *Nucl. Phys. A* **536**, 20 (1992).
- [26] J. O. Newton, *Prog. Nucl. Phys.* **4**, 234 (1955).
- [27] J. Randrup, C. F. Tsang, P. Möller, S. Nilsson, and S. E. Larsson, *Nucl. Phys. A* **217**, 221 (1973).
- [28] P. Lichtner, D. Drechsel, J. Maruhn, and W. Greiner, *Phys. Lett.* **45B**, 175 (1973).
- [29] J. F. Wild, J. van Aarle, W. Westmeier, R. W. Lougheed, E. K. Hulet, K. J. Moody, R. J. Dougan, E.-A. Koop, R. E. Glaser, R. Brandt, et al., *Phys. Rev. C* **41**, 640 (1990).
- [30] M. Brack, J. Damgaard, A. S. Jensen, H. C. Pauli, V. M. Strutinsky, and C. Y. Wong, *Rev. Mod. Phys.* **44**, 320 (1972).
- [31] J. Randrup, S. E. Larsson, P. Möller, S. G. Nilsson, K. Pomorski, and A. Sobczewski, *Phys. Rev. C* **13**, 229 (1976).
- [32] E. K. Hulet et al. :Data file EXFOR-13191.002 dated 1998-08-01, compare *Phys. Rev. C* **40**, 770 (1989). EXFOR data received from the IAEA Nuclear Data Section, Vienna.